

Spectral functions in functional renormalization group approach – analysis of the collective soft modes at the QCD critical point –

Takeru Yokota¹, Teiji Kunihiro¹ and Kenji Morita²

¹Department of Physics, Faculty of Science, Kyoto University, Kyoto 606-8502, Japan

²Yukawa Institute for Theoretical Physics, Kyoto University, Kyoto 606-8502, Japan

September 5, 2016

Abstract

We first review the method to calculate the spectral functions in the functional renormalization group (FRG) approach, which has been recently developed. We also provide the numerical stability conditions given by the present authors for a generic nonlinear evolution equation that are necessary for obtaining the accurate effective potential from the flow equation in the FRG. As an interesting example, we report the recent calculation of the spectral functions of the mesonic and particle-hole excitations using a chiral effective model of Quantum Chromodynamics (QCD); we extract the dispersion relations from them and try to reveal the nature of the soft modes at the QCD critical point (CP) where the phase transition is second order. Our result shows that a clear development and the softening of the phonon mode in the space-like region as the system approaches the CP; furthermore it turns out that the sigma mesonic mode once in the time-like region gets to merge with the phonon mode in the close vicinity of the CP, implying a novel possibility about the nature of the soft mode of the QCD CP.

1 Introduction

The functional renormalization group (FRG) [1–4] is a non-perturbative method of the field theory which enables us to investigate strongly correlated systems with incorporation of fluctuation effects beyond the mean-field theory. The FRG has been applied to a wide range of fields [5–14]. The FRG has proved powerful to study the equilibrium state of many-body systems or the nonperturbative vacuum of a quantum field theory. Elucidating dynamical properties of a physical system including possible emergence of collective excitations is important for fully understanding the physical properties of the system. It is to be noted that a phase change of the system can manifest itself as those in the properties of elementary excitations or more generally in the spectral functions in specific channels. Thus it is notable that the calculation of spectral functions has become possible in the framework of FRG [15–18], and hence one can extract the characteristics of system such as the possible development of collective modes and dispersion relations of modes [18].

Usually, the FRG applied to finite-temperature (T) systems is formulated in the imaginary-time formalism. A real-time analysis is, however, needed for extracting the spectral functions for excitation modes, which are essentially given as the imaginary part of the retarded Green's function, and an analytic continuation of two-point functions from imaginary Matsubara frequencies to real frequencies is made to have the real-time two-point Green's functions. It is, however, not a simple task and can be even quite intricate to perform an analytic continuation to get the spectral function in the nonperturbative method [19–22]. In the recent development [15–18], an unambiguous way of the analytic continuation has been proposed in the imaginary-time formalism, which has turned out to lead to reasonable results for the spectral functions in the $O(4)$ model in vacuum [15], in the quark-meson model at finite T and chemical potential μ [16, 17].

The method has been adopted with some adaptation to elucidate the nature of the soft modes of the critical point of Quantum Chromodynamics (QCD) at finite T and μ [18]. The QCD phase diagram, i.e. the phase diagram for the

system of quarks and gluons, is expected to have a rich structure and its clarification is one of the hot topics in the high-energy and nuclear physics [23]. The QCD Lagrangian reads

$$\mathcal{L}_{QCD} = \bar{\psi}(i\gamma_\mu D^\mu - \mathbf{m})\psi - \frac{1}{4}F_{\mu\nu}^a F^{\mu\nu a}$$

where $D_\mu = \partial_\mu - ig t^a A_\mu^a$ is the covariant derivative with A_μ^a being the gluon field with a color a ($a = 1, 2, \dots, N_c^2 - 1$). γ_μ denote Dirac matrices. Here $\mathbf{m} = \text{diag}(m_u, m_d, \dots)$ denotes the current quark mass matrix. One of the key concepts of QCD is the chiral symmetry, which is the invariance under the following independent two transformations (collectively called chiral transformation):

$$\psi_L \rightarrow \exp(i\theta_L^i T^i/2)\psi_L, \quad \psi_R \rightarrow \exp(i\theta_R^i T^i/2)\psi_R, \quad (1)$$

where the ψ_L and ψ_R are left- and right-handed quark fields, respectively, defined as $\psi_L = (1 - \gamma_5)\psi/2$ and $\psi_R = (1 + \gamma_5)\psi/2$ for quark field ψ with $\gamma_5 = i\gamma_0\gamma_1\gamma_2\gamma_3$. The matrix γ_5 has the eigenvalues ± 1 , which are called the chirality (handedness); $\psi_{L(R)}$ has the chirality -1 ($+1$), and hence the name of chiral symmetry. If we consider the N_f flavor case where the quark field $\psi = \psi^{fj}$ has N_f components as well as the color degrees of freedom ($j = 1, 2, \dots, N_c$), $\{T^i\}$ ($i = 0, \dots, N_f(N_f - 1)$) are the generators for $U(N_f)$ transformation for flavor index. θ_L^i and θ_R^i are real global parameters. Thus the transformations defined in (1) form a group $U(N_f)_L \otimes U(N_f)_R$ where the subscript L (R) is attached to discriminate the vector space to be transformed. The chiral group includes a subgroup $U_V(N_f) \simeq U_V(1) \otimes SU_V(N_f)$ which is realized when the constraint on the group parameters $\theta_L^i = \theta_R^i \equiv \theta^i$ ($i = 0, 1, 2, \dots, N_f(N_f - 1)$) is imposed: In fact, this transformation is simply represented in terms of the quark field ψ as $\psi \rightarrow \exp(i\theta^i T^i/2)\psi$. We can also define the transformation with another constraint $\theta_L^i = -\theta_R^i$, which is called $U_A(N_f) \simeq U_A(1) \otimes SU_A(N_f)$ transformation but does not form any group. If the current quark masses are ignored, the chiral symmetry becomes an exact symmetry of the (classical) QCD Lagrangian because the vector current is written in terms of left- and right-handed fields separately; $\bar{\psi}\gamma_\mu\psi = \bar{\psi}_L\gamma_\mu\psi_L + \bar{\psi}_R\gamma_\mu\psi_R$, in contrast to the Dirac mass term or scalar density $\bar{\psi}\psi = \bar{\psi}_R\psi_L + \bar{\psi}_L\psi_R$. One also readily sees that chiral symmetry is explicitly broken due to the current quark mass term $\bar{\psi}\mathbf{m}\psi$, although the neglect of this term is a good approximation in the low-energy regime for the lightest three flavors. An important remark is in order here: It turns out that the $U_A(1)$ symmetry is broken due to a quantum effect of QCD called axial or $U_A(1)$ anomaly [24]. Thus QCD in the quantum level has a $U_V(1) \otimes SU_V(N_f) \otimes SU_V(N_f)$ symmetry for the massless N_f flavors.

As Nambu first advocated [25, 26], the (approximate) chiral symmetry is spontaneously broken in the real world, and the pions are the massless bosons associated with the symmetry breaking (now called the Nambu-Goldstone bosons) with a small mass m_π acquired due to the small explicit breaking of the chiral symmetry for the two flavors. Indeed some low-energy theorem (Gell-Mann-Oakes-Renner relation [27]) tells us that the following formula holds;

$$f_\pi^2 m_\pi^2 = -\frac{1}{2}(m_u + m_d)\langle\bar{\psi}\psi\rangle,$$

where $f_\pi \simeq 93$ MeV is the pion decay constant with $\langle\bar{\psi}\psi\rangle \equiv \sigma_0$ denoting the vacuum expectation value of the (isoscalar) scalar density $\bar{\psi}\psi = \bar{u}u + \bar{d}d$. The existence of the finite scalar condensate (also called the chiral condensate) implies that chiral symmetry is spontaneously broken and the chiral condensate σ_0 can be regarded as an order parameter of the chiral transition of the QCD vacuum.

Apart from the chiral symmetry breaking, elementary excitations on top of the nonperturbative QCD vacuum are all color-singlet and called hadrons, which are the manifestation of the color confinement; colored quarks and gluons do not exist as asymptotic states. Thus at low-temperature and low-density regime, we have the confined phase with the chiral symmetry being spontaneously broken, which we call the hadronic phase. As in the usual many-body systems with a spontaneous symmetry breaking, the chiral symmetry is to be restored at high temperature and/or density where colors may be also liberated: Such a state of the matter is called a quark-gluon plasma (QGP).

Effective chiral models, i.e. models focusing on the chiral symmetry, has been utilized for an analysis of phase transitions in QCD. One of such models is the celebrated Nambu-Jona-Lasinio (NJL) model [26, 28]. In the case of $N_f = 2$, the model Lagrangian reads

$$\mathcal{L} = \bar{\psi}(i\partial\!\!\!/ - \mathbf{m})\psi + g\left[(\bar{\psi}\psi)^2 + (\bar{\psi}i\gamma_5\tau^a\psi)^2\right], \quad (2)$$

where g is a coupling constant, τ^a is the Pauli matrix and \mathbf{m} is a mass matrix. This model takes into account the axial anomaly and has $U_V(1) \otimes SU_V(2) \otimes SU_A(2)$ chiral symmetry except for the mass term.

A remarkable features in the expected phase structure is the possible existence of the first-order phase boundary between the hadronic phase and the QGP phase at large baryon chemical potential μ . In particular, the phase transition becomes second order at the end point of the first-order phase boundary, which is referred to the QCD CP.

In general, a system near the CP shows large fluctuations of and correlations between various quantities and thus a method beyond the mean-field theory is desirable for describing the physical properties near the CP. The FRG is expected to be a method to reveal the nature of the system more accurately than the mean-field theory and has been found to be useful in the description of chiral phase transition in QCD via effective chiral models [8–14]. Moreover, there exist specific collective modes which are coupled to the fluctuations of the order parameter and become gapless and a long-life at the CP. Such a mode is called the *soft mode* of the phase transition. As for the QCD CP, the nature of the soft modes is nontrivial due to the current quark mass [29, 30]. In the case of finite current quark mass, the universality class of the CP belongs to that of Z_2 CP and the soft mode is considered to be the particle-hole mode corresponding to the density (and energy) fluctuations. It is noteworthy that the scalar-vector coupling [31] caused by the finite quark mass at nonvanishing μ leads to a singular behavior of not only the chiral susceptibility but also susceptibilities of the hydrodynamical modes such as the density fluctuation or the quark-number susceptibility at the CP, as was shown in some model calculations [29, 30]. In Ref. [18], FRG has been applied to calculate the spectral functions of the sigma meson and pion channels, and thus the nature of the soft mode at the QCD CP was clarified.

In this lecture note, which is essentially a rearrangement of Ref. [18] with a focus on the technical part, we show the way to calculate the meson spectral functions in the two-flavor quark-meson model with FRG and its application to the analysis of the soft mode at the QCD CP. Our results confirm the softening of the particle-hole mode in the σ channel near the QCD CP, but not in the pion channel. In addition, we find that the low-momentum dispersion relation of sigma-mesonic mode penetrates into space-like region and the mode merges into the bump of the particle-hole mode.

This note is organized as follows. In Sec. 2, we recapitulate the method developed in [16, 17] and describe details for numerical calculation. The results are shown in Sec. 3. The phase diagram, the critical region and the precise location of the CP are presented in Sec. 3.1. In Sec. 3.3 the results of the spectral functions are shown, and the soft mode at the QCD CP is discussed. Sec. 4 is devoted to summary and outlook.

2 Method

In this section, we summarize the method to calculate the spectral functions in the FRG approach following Ref. [16, 17], and present a numerical stability condition [18] for solving the flow equation as an evolution equation. The method is applied to the two-flavor quark-meson model.

2.1 Procedure to derive spectral functions in meson channels

The FRG is based on the philosophy of the Wilsonian renormalization group [1–4] and realizes the coarse graining by introducing a regulator function R_k , which has a role to suppress modes with lower momentum than the scale k for the respective field. In this method, the effective average action (EAA) Γ_k is introduced such that it becomes bare action S_Λ at a large UV scale $k = \Lambda$ and becomes the effective action at $k \rightarrow 0$ with an appropriate choice of regulators. The flow equation for EAA, the Wetterich equation, can be derived as a functional differential equation [1]:

$$\partial_k \Gamma_k = \frac{1}{2} \text{STr} \left[\frac{\partial_k R_k}{\Gamma_k^{(2)} + R_k} \right], \quad (3)$$

where $\Gamma_k^{(n)}$ is the n -th functional derivative of Γ_k with respect to fields. This equation has a one-loop structure and can be represented diagrammatically as shown in Fig. 1 (a). In principle, one can get the effective action $\Gamma_{k=0}$ by solving Eq. (3) with the initial condition $\Gamma_\Lambda = S_\Lambda$.

The spectral function $\rho(\omega, p)$ for some field is derived from the imaginary part of the two-point retarded Green's function $G^R(\omega, p)$ for the field in momentum space:

$$\rho(\omega, p) = -\frac{1}{\pi} \text{Im} G^R(\omega, p). \quad (4)$$

Let us denote fields in a system as $\{\varphi_i\}$. Suppose that the average of $\{\varphi_i\}$, denoted by $\{\varphi_{i0}\}$, is obtained. Then, the inverse of the second derivative of the effective action at $\{\varphi_i = \varphi_{i0}\}$ leads to some two-point Green's function. In the imaginary-time formalism, the inverse of the second derivative of the effective action at $\{\varphi_i = \varphi_{i0}\}$ is the Matsubara Green's function and the analytic continuation from imaginary to real frequency in the momentum space gives the retarded Green's function if it retains the analyticity of the Green's function in the upper half-plane of complex frequency [32]. Therefore, one can get spectral functions by calculating second derivatives of EAA at $k = 0$ using Eq. (3). The flow equation for the second derivative of EAA is derived from Eq. (3) as

$$\begin{aligned} \partial_k \Gamma_{k,ij}^{(2)}[\varphi_0] = & \text{STr} \left[\left[\Gamma_k^{(2)} + R_k \right]_{ab}^{-1} \Gamma_{k,bci}^{(3)} \left[\Gamma_k^{(2)} + R_k \right]_{cd}^{-1} \Gamma_{k,dej}^{(3)} \left[\Gamma_k^{(2)} + R_k \right]_{ef}^{-1} \partial_k R_k^{fa} \right] \Big|_{\varphi=\varphi_0} \\ & - \frac{1}{2} \text{STr} \left[\left[\Gamma_k^{(2)} + R_k \right]_{ab}^{-1} \Gamma_{k,bcij}^{(4)} \left[\Gamma_k^{(2)} + R_k \right]_{cd}^{-1} \partial_k R_k^{da} \right] \Big|_{\varphi=\varphi_0}, \end{aligned} \quad (5)$$

where $\Gamma_{k,i_1 \dots i_n}^{(n)}$ represents the n th derivative of Γ_k with respect to $\varphi_{i_1}, \dots, \varphi_{i_n}$. The diagrammatic expression of this equation is shown in Fig. 1 (b). The RHS of Eq. (5) contains $\Gamma_k^{(2)}$, $\Gamma_k^{(3)}$ and $\Gamma_k^{(4)}$. In general the flow equation consists of an infinite hierarchy of differential equations such that the flow equation for $\Gamma_k^{(n)}$ contains $\Gamma_k^{(n+1)}$ and $\Gamma_k^{(n+2)}$. Some simplification of this hierarchy is needed to solve Eq. (5). One of the simplifications is evaluating the RHS of Eq. (5) with a truncated EAA and integrating the equation to $k = 0$. Adopting this simplification, we present the calculation of the meson spectral functions in the quark-meson model below.

We employ the two-flavor quark-meson model as the low-energy effective model of QCD. This is a chiral effective model consisting of the quark field and auxiliary fields σ and $\vec{\pi}$ corresponding to $\bar{q}q$ and $\bar{q}i\vec{\tau}\gamma_5 q$, respectively. We analyze in finite temperature and chemical potential. The bare action for this model in imaginary-time formalism is as follows:

$$S_\Lambda[\bar{\psi}, \psi, \phi] = \int_0^{\frac{1}{T}} d\tau \int d^3\vec{x} \left\{ \bar{\psi} (\not{\partial} + g_s(\sigma + i\vec{\tau} \cdot \vec{\pi}\gamma_5) - \mu\gamma_0) \psi + \frac{1}{2}(\partial_\mu \phi)^2 + V(\phi^2) - c\sigma \right\}, \quad (6)$$

where $\phi = (\sigma, \vec{\pi})$. The quark field ψ has the indices of four-component spinor, color $N_c = 3$ and flavor $N_f = 2$. The last term $c\sigma$ represents the effect of the current quark mass, which explicitly breaks chiral symmetry. $V(\phi^2)$ is the potential term of the mesons. We remark that the essential part of the meson-quark model (6) may be obtained by a Hubbard-Stratonovich transformation of the NJL model (2).

Now we take the local potential approximation (LPA) for the meson flow part as our truncation scheme. This truncation corresponds to considering only the lowest-order of derivative expansion for the meson flow part. Our truncated EAA is as follows [11]:

$$\Gamma_k[\bar{\psi}, \psi, \phi] = \int_0^{\frac{1}{T}} d\tau \int d^3x \left\{ \bar{\psi} (\not{\partial} + g_s(\sigma + i\vec{\tau} \cdot \vec{\pi}\gamma_5) - \mu\gamma_0) \psi + \frac{1}{2}(\partial_\mu \phi)^2 + U_k(\phi^2) - c\sigma \right\}, \quad (7)$$

where $U_k(\phi^2)$ satisfies $U_\Lambda(\phi^2) = V(\phi^2)$. In this truncation, we also neglect the flow of g_s and the wave function renormalization. Therefore, only the meson effective potential U_k has a k -dependence. The nonperturbative effects are to be incorporated through Eq. (5) with the truncated EAA used as the initial condition.

The procedure to calculate two-point functions is as follows. We first calculate the effective potential $U_k(\phi^2)$ using Eq. (3). Then the chiral condensate σ_0 , i.e., the average of σ , is obtained as σ satisfying the quantum equation of

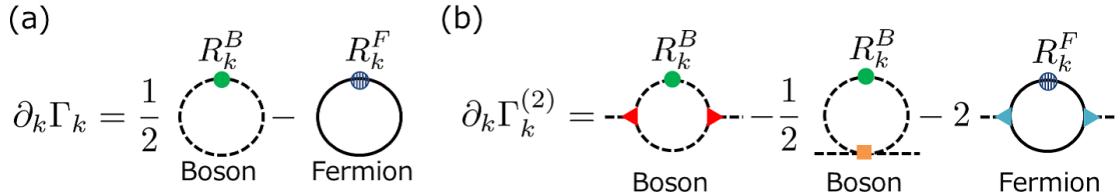


Figure 1: Diagrammatic representations of (a) Eq. (3) and (b) Eq. (5).

motion (EOM) $\delta\Gamma_{k=0}/\delta\sigma = 0$. In our case, this condition corresponds to obtaining σ that minimizes $U_k(\sigma^2) - c\sigma$, under the assumptions that the condensate is homogeneous and $\langle\vec{\pi}\rangle = \vec{0}$.

Next, we derive the flow equations for two-point Green's functions from Eq. (5). We define $\mathcal{G}_{k,\sigma}(P)$ and $\mathcal{G}_{k,\pi}(P)$ as

$$\left. \frac{\delta^2\Gamma_k}{\delta\sigma(P)\delta\sigma(Q)} \right|_{\vec{\psi}=0, \psi=0, \vec{\pi}=\vec{0}, \sigma=\sigma_0} = (2\pi)^4 \delta^{(4)}(P+Q) \mathcal{G}_{k,\sigma}^{-1}(P), \quad (8)$$

$$\left. \frac{\delta^2\Gamma_k}{\delta\pi_a(P)\delta\pi_a(Q)} \right|_{\vec{\psi}=0, \psi=0, \vec{\pi}=\vec{0}, \sigma=\sigma_0} = (2\pi)^4 \delta^{(4)}(P+Q) \mathcal{G}_{k,\pi}^{-1}(P), \quad (9)$$

where $\sigma(P)$ and $\pi_a(P)$ are the momentum space representations of the sigma and pion fields, respectively, and $P = (i\omega_n, \vec{p})$ with ω_n being the bosonic Matsubara frequency. These quantities become Matsubara Green's functions at $k = 0$. By inserting the average values $\sigma = \sigma_0$, $\vec{\pi} = \vec{0}$, and $\vec{\psi} = \psi = 0$ and choosing $\varphi_i = \sigma(P)$ and $\varphi_j = \sigma(Q)$ ($\varphi_i = \pi_a(P)$ and $\varphi_j = \pi_a(Q)$) in Eq. (5), the flow equation for $\mathcal{G}_{k,\sigma}(P)$ ($\mathcal{G}_{k,\pi}(P)$) can be obtained. In our approximation, the $\Gamma_k^{(2)}$, $\Gamma_k^{(3)}$ and $\Gamma_k^{(4)}$ in the RHS of Eq. (5) are evaluated using Eq. (7).

We define $G_{k,\sigma}^R(P)$ ($G_{k,\pi}^R(P)$) as the function which is obtained by analytic continuation for $\mathcal{G}_{k,\sigma}(P)$ ($\mathcal{G}_{k,\pi}(P)$) from imaginary Matsubara frequencies to real frequencies retaining the analyticity in the upper half-plane of complex frequency. The solutions of $G_{k,\sigma}^R(P)$ and $G_{k,\pi}^R(P)$ at $k = 0$ give the retarded Green's functions in the sigma and pion channel, respectively. Therefore, if analytic continuation of the flow equations for $\mathcal{G}_{k,\sigma}(P)$ ($\mathcal{G}_{k,\pi}(P)$) is performed and the flow equation for $G_{k,\sigma}^R(P)$ ($G_{k,\pi}^R(P)$) is obtained, one can calculate the retarded Green's function using the flow equation. In our case, such an analytic continuation is successfully carried as follows: As mentioned above, the analyticity of the Green's function in the upper half-plane of ω must be retained. In the present case, the flow equation itself should be analytic in the upper half-plane after the analytic continuation. One can retain the analyticity in the upper half-plane easily by taking into account the following points.

1. By choosing ω_n -independent regulators, one can avoid possible extra poles in the ω plane in the flow equation otherwise arising from ω_n dependence of the regulators.
2. The next point is about the analytic continuation of thermal distribution functions $n_{B,F}(E + i\omega_n)$ obtained for a discrete (multiple of $2\pi T$) frequency ω_n , where the subscript B, F stands for a boson or fermion, respectively, and E is ω_n independent. Such factors appear in the flow equation after the Matsubara summation. Because of the periodicity of the exponential function, $n_{B,F}(E + i\omega_n)$ is equal to $n_{B,F}(E)$. However if $n_{B,F}(E + \omega)$ is substituted for $n_{B,F}(E + i\omega_n)$, such a factor breaks the analyticity of the flow equation in the upper half-plane. Therefore $n_{B,F}(E + i\omega_n)$ should be replaced by $n_{B,F}(E)$ before the analytic continuation.

By taking into account these points, the substitution $\omega + i\epsilon$ for $i\omega_n$ with ϵ being a positive infinitesimal gives the flow equations for $G_{k,\sigma}^R(P)$ and $G_{k,\pi}^R(P)$.

Finally, the spectral functions in the meson channels are given in terms of the thus-obtained retarded Green's functions $G_{k \rightarrow 0, \sigma}^R(P)$ and $G_{k \rightarrow 0, \pi}^R(P)$ using Eq. (4).

2.2 Flow equations

In the present work, we adopt the 3D Litim's optimized regulators for bosons and fermions [33] as ω_n -independent regulators:

$$R_k^B(Q) = (k^2 - \vec{q}^2)\theta(k^2 - \vec{q}^2), \quad (10)$$

$$R_k^F(Q) = i\vec{q} \left(\sqrt{\frac{k^2}{\vec{q}^2}} - 1 \right) \theta(k^2 - \vec{q}^2). \quad (11)$$

Then the insertion of Eq. (7) into Eq. (3) leads to the following flow equation for U_k :

$$\partial_t U_k = \frac{k^5}{12\pi^2} \left[-2N_f N_c \left[\frac{1}{E_\psi} \tanh \frac{E_\psi + \mu}{2T} + \frac{1}{E_\psi} \tanh \frac{E_\psi - \mu}{2T} \right] + \frac{1}{E_\sigma} \coth \frac{E_\sigma}{2T} + \frac{3}{E_\pi} \coth \frac{E_\pi}{2T} \right], \quad (12)$$

where $t = \ln(k/\Lambda)$, $E_a = \sqrt{k^2 + m_a^2}$ ($a = \psi, \sigma, \pi$), and

$$m_\psi^2 = g_s^2 \sigma^2, \quad m_\sigma^2 = \partial_\sigma^2 U_k, \quad m_\pi^2 = \partial_\sigma U_k / \sigma. \quad (13)$$

According to the procedure presented in the previous subsection, the flow equations for $\Gamma_{k,\sigma}^{(2)}(P)$ and $\Gamma_{k,\pi}^{(2)}(P)$ become:

$$\partial_k \Gamma_{k,\sigma}^{(2)}(P) = J_{k,\sigma\sigma}(P)(\Gamma_{k,\sigma\sigma}^{(0,3)})^2 - \frac{1}{2} I_{k,\sigma}^{(2)} \Gamma_{k,\sigma\sigma\sigma}^{(0,4)} + 3J_{k,\pi\pi}(P)(\Gamma_{k,\pi\pi}^{(0,3)})^2 - \frac{3}{2} I_{k,\pi}^{(2)} \Gamma_{k,\sigma\sigma\pi\pi}^{(0,4)} - 2N_c N_f J_{k,\bar{\psi}\psi}^{(\sigma)}(P), \quad (14)$$

$$\partial_k \Gamma_{k,\pi}^{(2)}(P) = J_{k,\sigma\pi}(P)(\Gamma_{k,\sigma\pi}^{(0,3)})^2 + J_{k,\pi\sigma}(P)(\Gamma_{k,\sigma\pi\pi}^{(0,3)})^2 - \frac{1}{2} I_{k,\sigma}^{(2)} \Gamma_{k,\sigma\sigma\pi\pi}^{(0,4)} - \frac{5}{2} I_{k,\pi}^{(2)} \Gamma_{k,\pi\pi\tilde{\pi}\pi}^{(0,4)} - 2N_c N_f J_{k,\bar{\psi}\psi}^{(\pi)}(P), \quad (15)$$

respectively, where $\pi, \tilde{\pi} \in \{\pi_1, \pi_2, \pi_3\}$ and $\pi \neq \tilde{\pi}$. The loop-functions $J_{k,\alpha\beta}(P)$, $I_{k,\alpha}^{(2)}$, and $J_{k,\bar{\psi}\psi}^{(\alpha)}(P)$ ($\alpha, \beta = \sigma, \pi$) are defined as

$$J_{k,\alpha\beta}(P) = T \sum_{q_n} \int \frac{d^3 \vec{q}}{(2\pi)^3} \partial_k R_k^B(q) G_{k,\alpha}^B(P)^2 G_{k,\beta}^B(Q - P), \quad (16)$$

$$I_{k,\alpha}^{(2)} = T \sum_{q_n} \int \frac{d^3 \vec{q}}{(2\pi)^3} \partial_k R_k^B(q) G_{k,\alpha}^B(Q)^2, \quad (17)$$

$$J_{k,\bar{\psi}\psi}^{(\alpha)}(P) = T \sum_{q_n} \int \frac{d^3 \vec{q}}{(2\pi)^3} \text{tr} \left[\Gamma_{\bar{\psi}\psi\alpha}^{(2,1)} G_{k,\bar{\psi}\psi}^F(Q) \partial_k R_k^F(Q) G_{k,\bar{\psi}\psi}^F(Q) \Gamma_{\bar{\psi}\psi\alpha}^{(2,1)} G_{k,\bar{\psi}\psi}^F(Q - P) \right], \quad (18)$$

where $Q = (iq_n, \vec{q})$ and

$$G_{k,\alpha}^B(Q) = \left[Q^2 + m_\alpha^2 \Big|_{\sigma=\sigma_0} + R_k^B(Q) \right]^{-1}, \quad (19)$$

$$G_{k,\bar{\psi}\psi}^F(Q) = \left[\not{Q} - \mu\gamma_0 + m_\psi \Big|_{\sigma=\sigma_0} + R_k^F(Q) \right]^{-1}. \quad (20)$$

The three- and four-point vertices $\Gamma_{\bar{\psi}\psi\phi_i}^{(2,1)}$, $\Gamma_{k,\phi_i\phi_j\phi_l}^{(0,3)}$, and $\Gamma_{k,\phi_i\phi_j\phi_l\phi_m}^{(0,4)}$ are defined as

$$\frac{\delta}{\delta\phi_i(P_1)} \frac{\overrightarrow{\delta}}{\delta\bar{\psi}(P_2)} \Gamma_k \frac{\overleftarrow{\delta}}{\delta\psi(P_3)} = (2\pi)^4 \delta^{(4)}(P_1 + P_2 + P_3) \Gamma_{\bar{\psi}\psi\phi_i}^{(2,1)}, \quad (21)$$

$$\frac{\delta^3 \Gamma_k}{\delta\phi_i(P_1) \delta\phi_j(P_2) \delta\phi_l(P_3)} = (2\pi)^4 \delta^{(4)}(P_1 + P_2 + P_3) \Gamma_{k,\phi_i\phi_j\phi_l}^{(0,3)}, \quad (22)$$

$$\frac{\delta^4 \Gamma_k}{\delta\phi_i(P_1) \delta\phi_j(P_2) \delta\phi_l(P_3) \delta\phi_m(P_4)} = (2\pi)^4 \delta^{(4)}(P_1 + P_2 + P_3 + P_4) \Gamma_{k,\phi_i\phi_j\phi_l\phi_m}^{(0,4)}, \quad (23)$$

some of which are expressed in terms of U_k :

$$\Gamma_{\bar{\psi}\psi\phi_i}^{(2,1)} = \begin{cases} g_s & (\text{for } i = 0) \\ g_s i\gamma^5 \tau^i & (\text{for } i = 1, 2, 3) \end{cases}, \quad (24)$$

$$\Gamma_{k,\phi_i\phi_j\phi_l}^{(0,3)} = 4U_k^{(2)} (\delta_{ij}\phi_m + \delta_{im}\phi_j + \delta_{jm}\phi_i) + 8U_k^{(3)} \phi_i\phi_j\phi_m, \quad (25)$$

$$\begin{aligned} \Gamma_{k,\phi_i\phi_j\phi_l\phi_m}^{(0,4)} &= 4U_k^{(3)} (\delta_{ij}\delta_{mn} + \delta_{in}\delta_{jm} + \delta_{jn}\delta_{im}) \\ &\quad + 8U_k^{(3)} (\delta_{ij}\phi_l\phi_m + \delta_{jl}\phi_i\phi_m + \delta_{lm}\phi_i\phi_j + \delta_{jm}\phi_i\phi_l + \delta_{im}\phi_j\phi_l + \delta_{il}\phi_j\phi_m) \\ &\quad + 16U_k^{(4)} \phi_i\phi_j\phi_l\phi_m. \end{aligned} \quad (26)$$

Analytic continuation in Eq. (14) and Eq. (15) is carried out after the Matsubara summation in Eqs. (16)–(18). The explicit forms of Eq. (16) - (18) after Matsubara summation is shown in [18].

To solve these flow equations, we employ the following initial conditions at the UV scale $k = \Lambda$:

$$U_\Lambda(\phi^2) = V(\phi^2) = \frac{1}{2}m_\Lambda^2\phi^2 + \frac{1}{4}\lambda_\Lambda(\phi^2)^2, \quad (27)$$

$$\Gamma_{\Lambda,\sigma}^{(2),R}(\omega, \vec{p}) = -\omega^2 + \vec{p}^2 + \partial_\sigma^2 U_\Lambda(\sigma_0^2), \quad (28)$$

$$\Gamma_{\Lambda,\pi}^{(2),R}(\omega, \vec{p}) = -\omega^2 + \vec{p}^2 + \partial_\sigma U_\Lambda(\sigma_0^2)/\sigma_0. \quad (29)$$

2.3 Numerical stability conditions

We employ the grid method to solve Eq. (12) numerically. This method reveals the global structure of $U_k(\sigma^2)$ on discretized σ . We employ the fourth-order Runge-Kutta method to solve Eq. (12).

In general when one solves a partial differential equation numerically, the discretization of derivatives may cause numerical errors. Thus, one needs to impose numerical stability conditions to avoid the enhancement of the error due to accumulation. The derivation of such conditions is concretely demonstrated in the case of linear partial differential equations and briefly mentioned in the case of nonlinear partial differential equations in [34].

A numerical stability conditions for numerical calculation was given for the following partial differential equation in [18]:

$$\frac{\partial u(t, \sigma)}{\partial t} = f\left(t, \sigma, u(t, \sigma), \frac{\partial u(t, \sigma)}{\partial \sigma}, \frac{\partial^2 u(t, \sigma)}{\partial \sigma^2}\right). \quad (30)$$

where f is an arbitrary real function. This equation is a generalized equation of Eq. (12). The equation to describe the evolution of numerical deviation for $u(t, \sigma)$ can be derived from the discretized form of Eq. (30) for t and σ , from which one can derive the conditions for suppressing the amplification of the numerical deviation, i.e., the numerical stability conditions. If we choose forward difference for t -derivative and central three-point difference for σ -derivative as the discretization the stability conditions for Eq. (30) are as follows [18]:

$$\begin{cases} |\Delta t| \leq \frac{2|G|}{F^2}, \\ |\Delta t| \leq \frac{\Delta \sigma^2}{2|G|}, \end{cases} \quad (31)$$

where

$$F \equiv \frac{\partial f}{\partial u'}, \quad G \equiv \frac{\partial f}{\partial u''} \left(u' = \frac{\partial u}{\partial \sigma}, u'' = \frac{\partial^2 u}{\partial \sigma^2} \right).$$

In the case of Eq. (12), t and $u(t, \sigma)$ are identified with $\ln(k/\Lambda)$ and $U_k(\sigma^2)$, respectively, and F and G are derived to be:

$$\begin{cases} F = -\frac{k^5}{8\pi^2\sigma E_\sigma^3} \left(\coth \frac{E_\pi}{2T} + \frac{E_\pi}{2T} \frac{1}{\sinh^2 \frac{E_\pi}{2T}} \right), \\ G = -\frac{k^5}{24\pi^2 E_\sigma^3} \frac{\coth \frac{E_\pi}{2T} + \frac{E_\pi}{2T} \frac{1}{\sinh^2 \frac{E_\pi}{2T}}}{\left(\coth \frac{E_\pi}{2T} + \frac{E_\pi}{2T} \frac{1}{\sinh^2 \frac{E_\pi}{2T}} \right)^2}. \end{cases} \quad (32)$$

$$\quad (33)$$

G is negative definite, and Δt is also negative because the direction of flow is from $k = \Lambda$ to $k = 0$.

We fix the intervals of discretization of σ and t in Eq. (12) according to these conditions. Because the above condition of Eq. (31) is too strict when σ is close to zero, we neglect the condition around $\sigma = 0$ in practice.

2.4 Other numerical details

As stated before, the flow equation (12) should be integrated down to $k = 0$ from $k = \Lambda$ to get the effective action $\Gamma_{k=0}$ in principle. However, due to the conditions for stable calculation mentioned above, solving the flow equation to small k is quite time-consuming for some regions of the (T, μ) plane, such as the low-temperature region of the hadronic

phase. In such a region, the curvature of U_k , i.e., m_σ^2 , can take a negative value, which leads to small E_σ for some σ . This gives large F and $|G|$ (Eqs.(32) and (33)) as k decreases and the condition (31) becomes difficult to satisfy at small k . Thus, some infrared scale $k = k_{\text{IR}}$ is introduced in practice, at which the numerical procedure is stopped. Of course, k_{IR} should be as small as possible so that sufficiently low-momentum fluctuations are taken into account to describe the system around the CP where vanishingly low-momentum excitations exist. Thus we choose a much lower value of k_{IR} than the 40 MeV adopted in Ref. [17], and set $k_{\text{IR}} = 1$ MeV as being small enough to incorporate the low-momentum fluctuations. Therefore our calculation will be reliable in the vicinity of the CP, except for the small surrounding region where excitation modes with momentum scales lower than 1 MeV are strongly developed. Although ϵ , which appears after the analytic continuation, is defined as a positive infinitesimal, we set it to 1 MeV in the present calculation, which should be small enough for present purposes.

3D momentum integrals remain after the Matsubara summation in Eq. (14) and Eq. (15). These integrals can be fully calculated analytically for zero external momentum. Even for a finite external momentum, they can be nicely reduced to 1D integrals, which are evaluated numerically. The numerical integrations involve a tricky point, and one has to take care of the poles of each term in the integrands. As an example, we show the explicit form of $J_{k,\alpha\beta}(P)$ after Matsubara summation:

$$J_{k,\alpha\beta}(P) = \int_{D_1} \frac{d^3q}{(2\pi)^3} \frac{k}{2} \left[(1 + n_B(E_\alpha)) \frac{E_\alpha^2 + E_\beta^2 - (2E_\alpha + ip_0)^2}{E_\alpha^3(E_\beta^2 - (E_\alpha + ip_0)^2)^2} + n_B(E_\alpha) \frac{E_\alpha^2 + E_\beta^2 - (2E_\alpha - ip_0)^2}{E_\alpha^3(E_\beta^2 - (E_\alpha - ip_0)^2)^2} \right. \\ \left. + \frac{2(1 + n_B(E_\beta))}{E_\beta(E_\alpha^2 - (E_\beta - ip_0)^2)^2} + \frac{2n_B(E_\beta)}{E_\beta(E_\alpha^2 - (E_\beta + ip_0)^2)^2} - \frac{n'_B(E_\alpha)}{E_\alpha^2(E_\beta^2 - (E_\alpha - ip_0)^2)} - \frac{n'_B(E_\alpha)}{E_\alpha^2(E_\beta^2 - (E_\alpha + ip_0)^2)} \right] \\ + \int_{D_2} \frac{d^3q}{(2\pi)^3} \frac{k}{2} \left[(1 + n_B(E_\alpha)) \frac{E_\alpha^2 + \tilde{E}_\beta^2 - (2E_\alpha + ip_0)^2}{E_\alpha^3(\tilde{E}_\beta^2 - (E_\alpha + ip_0)^2)^2} + n_B(E_\alpha) \frac{E_\alpha^2 + \tilde{E}_\beta^2 - (2E_\alpha - ip_0)^2}{E_\alpha^3(\tilde{E}_\beta^2 - (E_\alpha - ip_0)^2)^2} \right. \\ \left. + \frac{2(1 + n_B(\tilde{E}_\beta))}{\tilde{E}_\beta(E_\alpha^2 - (\tilde{E}_\beta - ip_0)^2)^2} + \frac{2n_B(\tilde{E}_\beta)}{\tilde{E}_\beta(E_\alpha^2 - (\tilde{E}_\beta + ip_0)^2)^2} - \frac{n'_B(E_\alpha)}{E_\alpha^2(\tilde{E}_\beta^2 - (E_\alpha - ip_0)^2)} - \frac{n'_B(E_\alpha)}{E_\alpha^2(\tilde{E}_\beta^2 - (E_\alpha + ip_0)^2)} \right], \quad (34)$$

where $E_\alpha = \sqrt{k^2 + m_\alpha^2}$, $\tilde{E}_\alpha = \sqrt{\vec{q}^2 + m_\alpha^2}$, $n'_{B,F}(E) = dn_{B,F}(E)/dE$,

$$D_1 = \left\{ \vec{q} \in \mathbb{R}^3 \mid |\vec{q} - \vec{p}| < k \text{ and } |\vec{q}| < k \right\}, \quad D_2 = \left\{ \vec{q} \in \mathbb{R}^3 \mid |\vec{q} - \vec{p}| < k \text{ and } |\vec{q}| > k \right\},$$

and $ip_0 = \omega + i\epsilon$. The first and the third terms of the integrand of the second integral in Eq. (34) have the same pole $\tilde{E}_\alpha = E_\alpha + ip_0$. If such terms are integrated separately, a large cancellation can occur, which then leads to big numerical errors. Therefore, we first combine such terms analytically in the integrand before numerical integrations.

2.5 Parameter setting

The truncated EAA Eq. (7) and the initial condition Eq. (27) have some parameters which are fixed so as to reproduce the observables in vacuum: We use the same values of the parameters as those in [17] and list them in Table 1.

The chiral condensate σ_0 is determined as σ which minimize $U_k(\sigma^2) - c\sigma$ and the constituent quark mass M_ψ and the sigma and pion screening masses M_σ and M_π are calculated using Eq. (13):

$$M_a = \left(m_a^2 \Big|_{\sigma=\sigma_0, k=k_{\text{IR}}} \right)^{\frac{1}{2}}, \quad (a = \psi, \sigma, \pi). \quad (35)$$

Our parameters reproduce $\sigma_0 = 93\text{MeV}$, $M_q = 286\text{MeV}$, $M_\pi = 137\text{MeV}$ and $M_\sigma = 496\text{MeV}$ in vacuum.

3 Results

3.1 Phase diagram

We show the phase diagram on temperature (T) and chemical potential (μ) plane in Fig. 2, where a contour map of the chiral condensate is also given. One sees that chiral restoration occurs as the temperature is raised, and the phase

Λ	m_Λ/Λ	λ_Λ	c/Λ^3	g_s
1000MeV	0.794	2.00	0.00175	3.2

Table 1: Used values of Λ and the parameters in the initial condition $\Gamma_{k=\Lambda}$ used in the calculation.

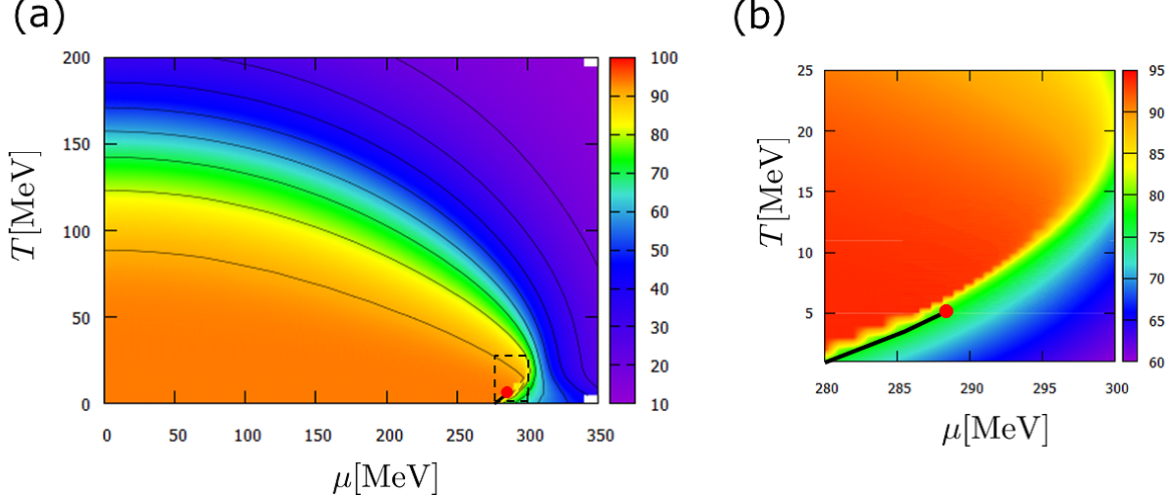


Figure 2: (a) Contour map of the chiral condensate σ_0 . (b) Enlargement of the area surrounded by dotted lines in (a). The filled circle (red) is the CP and the solid (black) line is the first-order phase boundary. (Taken from [18])

transition is not a genuine one but a crossover, except for the low-temperature and large chemical potential region, where the phase transition is of first order. This feature is qualitatively in accordance with the results given in the literature, although the location of the CP here is in a somewhat smaller temperature region than that given in Ref. [17]. The detailed procedure for locating the CP is described below.

At the QCD CP, the chiral susceptibility diverges. Therefore, we locate the CP by searching for the point where the sigma screening mass M_σ , the square of which is the inverse of the chiral susceptibility, becomes the smallest: We seek the minimum position of M_σ using the data points where M_σ is greater than 1 MeV, because our choice of $k_{\text{IR}} = 1$ MeV enables us to take into account fluctuations whose momentum scales are greater than k_{IR} so as to make the result of M_σ reliable when M_σ is larger than 1 MeV. We also identify the first-order phase transition by a discontinuity of the chiral condensate. The results at $T = 5.0$ MeV, 5.1 MeV, and 5.2 MeV are shown in Fig. 3 as functions of $\mu - \mu_t(T)$, where $\mu_t(T)$ is the transition chemical potential for each temperature determined by the minimum point of the sigma curvature mass and is found to be $\mu_t(5.0 \text{ MeV}) = 286.517 \text{ 02 MeV}$, $\mu_t(5.1 \text{ MeV}) = 286.686 \text{ 00 MeV}$, and $\mu_t(5.2 \text{ MeV}) = 286.853 \text{ 20 MeV}$.

We find that the sigma screening mass becomes smallest between $T = 5.0$ MeV and $T = 5.2$ MeV and between $\mu = \mu_t(5.0 \text{ MeV})$ and $\mu = \mu_t(5.2 \text{ MeV})$. Therefore, the critical temperature T_c and the critical chemical potential μ_c are estimated as $T_c = 5.1 \pm 0.1$ MeV and $\mu_c = 286.6 \pm 0.2$ MeV. The position of the CP is quite different from the $(T, \mu) = (10 \text{ MeV}, 292.97 \text{ MeV})$ given in Ref. [17]. Such a difference may be attributed to the different choice of k_{IR} . In the following discussion, we regard T_c and μ_c as 5.1 MeV and 286.686 MeV, respectively. As seen in the behavior of the chiral condensate shown in the right panel of Fig. 3, the phase transition along the chemical potential is of first order when $T = 5.0$ MeV and a crossover when $T = 5.2$ MeV.

3.2 Examples of the results of the spectral function in the σ channel

We first show examples of the results of the spectral function in the σ channel $\rho_\sigma(\omega, p)$. Figure 4 is the result of $\rho_\sigma(\omega, p)$ at $(T, \mu) = (5.1 \text{ MeV}, 286.3 \text{ MeV})$. There is a sharp peak at $\omega = 250 \text{ MeV}$ and a relatively small bump in the

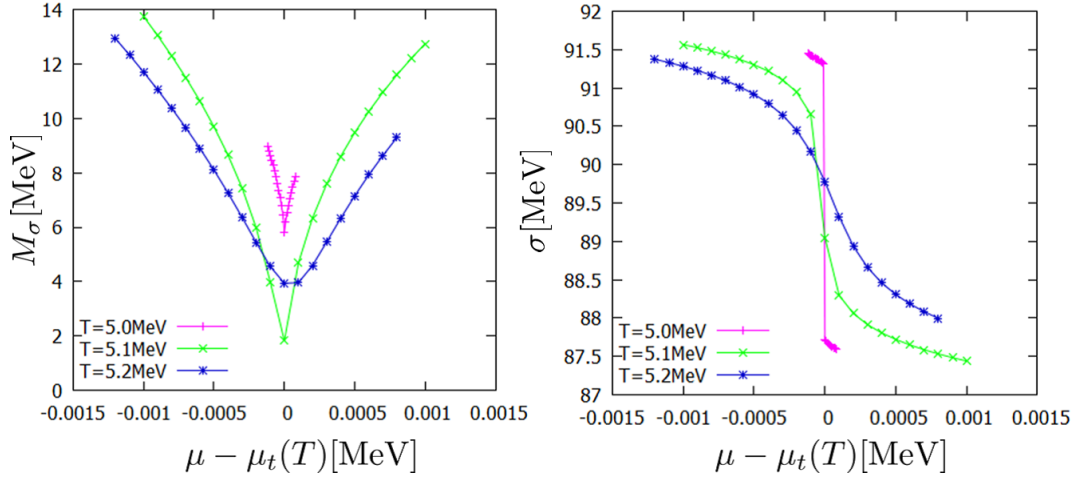


Figure 3: The sigma curvature masses M_σ and the chiral condensates σ_0 at $T = 5.0$ MeV, 5.1 MeV, and 5.2 MeV. (Taken from [18])

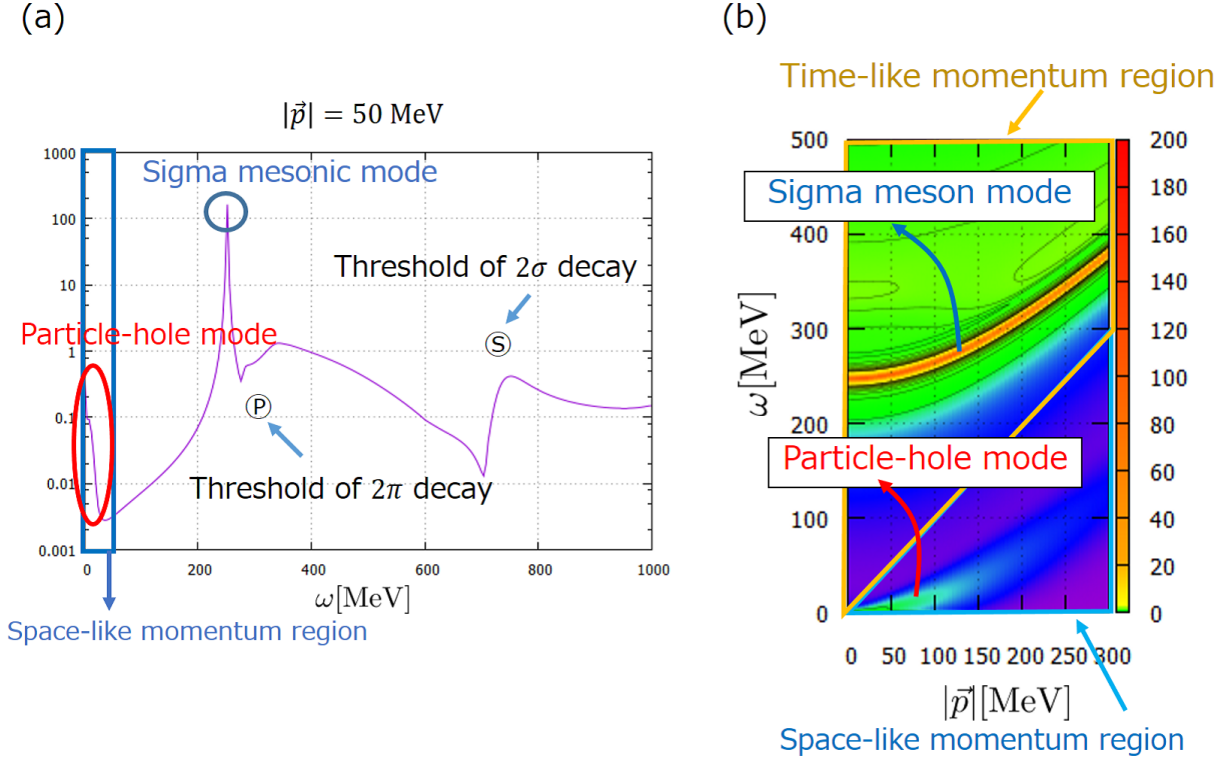


Figure 4: An example of results of $\rho_\sigma(\omega, p)$: (a) the result when $|\vec{p}| = 50$ MeV at $(T, \mu) = (5.1 \text{ MeV}, 286.3 \text{ MeV})$ and (b) the contour map of $\rho_\sigma(\omega, p)$ at the same temperature and chemical potential. In (a), the positions of the thresholds for 2σ and 2π decay channel determined by Eq. (36) are denoted by \textcircled{S} , \textcircled{P} .

space-like region $\omega < p$ in Fig. 4(a): They correspond to the sigma meson with a modified mass at finite temperature and the phonon mode composed of particle-hole excitations, respectively, which is in accord with the result in RPA

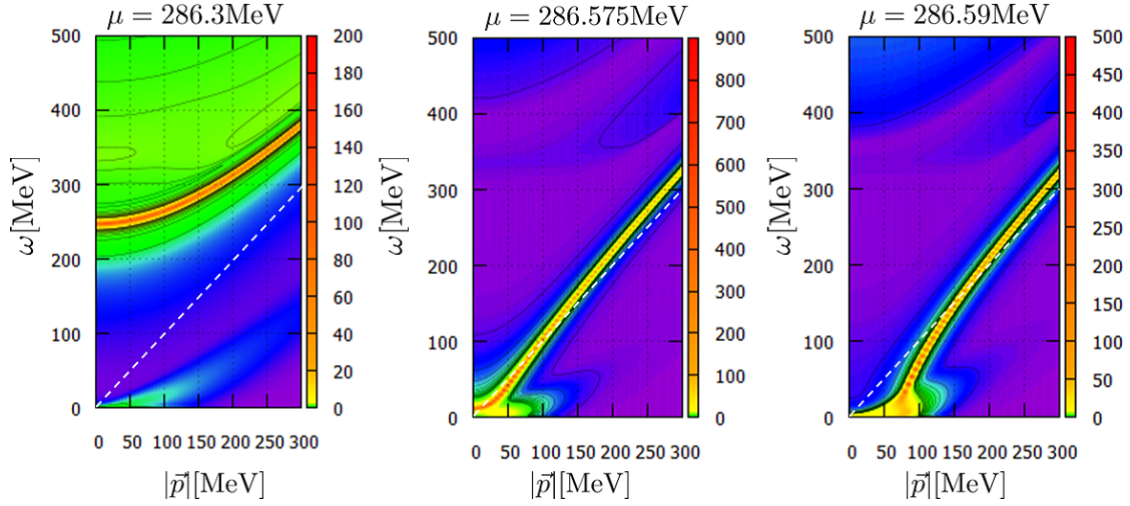


Figure 5: Contour maps of ρ_σ at $T = T_c$ and $\mu = 286.3\text{MeV}$, 286.575MeV and 286.59MeV . (Taken from [18])

in [29]. In Fig. 4(b), the dispersion relations of the sigma meson mode and particle-hole mode can be seen clearly.

The spectral function also tells us the decay and absorption processes of the particle excitations from the width of the corresponding peaks or bumps. In our energy scale, the following processes contribute to the spectral function $\rho_\sigma(\omega, \vec{p})$:

$$\sigma^* \rightarrow \sigma\sigma, \quad \sigma^* \rightarrow \pi\pi, \quad \sigma^* \rightarrow \bar{\psi}\psi, \quad \sigma^*\sigma \rightarrow \sigma, \quad \sigma^*\pi \rightarrow \pi, \quad \sigma^*\psi \rightarrow \psi,$$

where σ^* denotes a virtual state in the sigma channel with energy-momentum (ω, \vec{p}) . The energy-momentum conservation gives constraints on the possible (ω, \vec{p}) region for the former three processes as follows:

$$\begin{aligned} \omega &\geq \sqrt{\vec{p}^2 + (2M_\sigma)^2} \quad \text{for } \sigma^* \rightarrow \sigma\sigma, \\ \omega &\geq \sqrt{\vec{p}^2 + (2M_\pi)^2} \quad \text{for } \sigma^* \rightarrow \pi\pi, \\ \omega &\geq \sqrt{\vec{p}^2 + (2M_\psi)^2} \quad \text{for } \sigma^* \rightarrow \bar{\psi}\psi, \end{aligned} \tag{36}$$

which are all in the time-like region. On the other hand, the latter three processes are all collisional ones and possible only in the space-like region, $0 \leq \omega < p$. In particular, the last process $\sigma^*\psi \rightarrow \psi$ corresponds to the absorption process of the σ^* mode into a thermally excited quark. In Fig. 4(a), the positions of the thresholds for 2σ and 2π decay channel determined by Eq. (36) are shown, and the bumps corresponding to these processes can be seen.

3.3 Spectral functions near the QCD CP

We calculate the spectral function in the σ channel near the QCD CP, by increasing the chemical potential toward μ_c along constant temperature line $T = T_c$. As seen in Sec. 3.2, we can see the dispersion relations of the modes by making contour maps of the spectral functions as functions of ω and p . Figure 5 shows the dispersion relations of the sigma meson and particle-hole modes near the CP. At $\mu = 286.3\text{MeV}$, the sigma-mesonic peaks can be seen in the time-like region as well as the particle-hole bump in the space-like region. As the chemical potential increases, the dispersion relation of the sigma-mesonic mode shifts downward and it touches the light cone near $\mu = 286.575\text{MeV}$. At $\mu = 286.59\text{MeV}$, in low-momentum region the sigma-mesonic mode clearly penetrates into space-like region and merges to the particle-hole bump, which has a flat dispersion relation in the small momentum region.

Next, we show the strength of peaks and bumps of the spectral function when p is set to 50MeV . The results at $\mu = 286.00\text{MeV}$, $\mu = 286.50\text{MeV}$ and $\mu = 286.57\text{MeV}$ are shown in Fig. 6 (a). One can see the sigma-mesonic peak as well as bumps corresponding to 2σ and 2π decay in the time-like region. The peak position of the sigma-mesonic mode shifts to the lower energy as the system approaches the CP. The position of the 2σ threshold also shifts

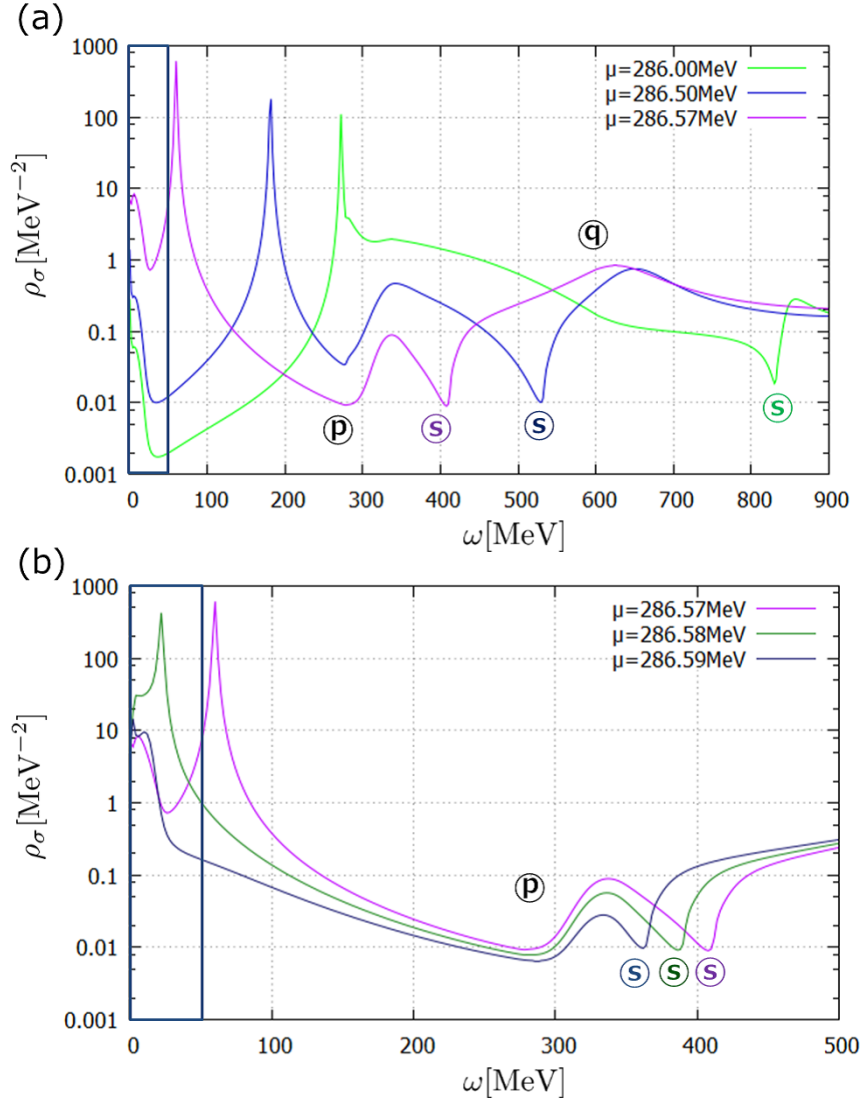


Figure 6: ρ_σ near the QCD CP at $T = T_c$: (a) the results in $286.00 \text{ MeV} \leq \mu \leq 286.57 \text{ MeV}$ and (b) the results in $286.57 \text{ MeV} \leq \mu \leq 286.59 \text{ MeV}$. The spatial momentum is set to $p = 50 \text{ MeV}$ and the inside of the blue box in each figure is the space-like region. The 2σ decay thresholds for each chemical potential are denoted by Ⓢ. The 2π and $\bar{\psi}\psi$ decay thresholds hardly change and are represented by Ⓟ and Ⓠ. (Taken from [18])

to a lower energy while those of the 2π and $\bar{\psi}\psi$ thresholds hardly change. The spectral function in the space-like region is drastically enhanced as the system is close to the CP. This behavior can be interpreted as the softening of the particle-hole mode. In Fig. 6(b), we show the results at chemical potentials much closer to the CP. Because of numerical instability in $286.60 \text{ MeV} \leq \mu \leq 360 \text{ MeV}$, we choose $\mu = 286.58 \text{ MeV}$ and $\mu = 286.59 \text{ MeV}$. For comparison, the result at $\mu = 286.57 \text{ MeV}$ is also shown. These results are quite different from those in $\mu \leq 286.57 \text{ MeV}$. In $\mu > 286.57 \text{ MeV}$, the peak of the sigma-mesonic mode penetrates into the space-like region and then merges into the particle-hole mode. Our results indicate that the sigma-mesonic mode as well as the particle-hole mode can become soft near the CP.

One of the possible triggers of this phenomenon is the level repulsion between the sigma-mesonic mode and other modes. In particular, the two-sigma ($\sigma\sigma$) mode is considered to play an important role in the level repulsion since the threshold of the two-sigma mode shifts downward as the system approaches the CP. Let us suppose that the particle-

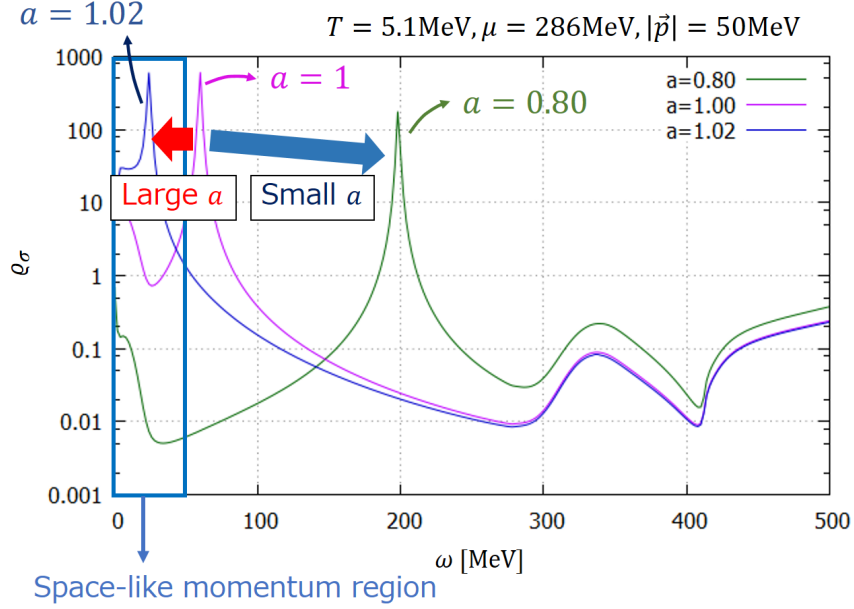


Figure 7: ρ_σ with a substituted three-point vertex $a\Gamma_{k,\sigma\sigma\sigma}^{(3)}$ at $T = T_c$, $\mu = 286.57$ MeV, and $p = 50$ MeV. The inside of the blue box is the space-like region.

hole mode, the sigma-mesonic mode, and the two-sigma mode can each be described by a state having a single energy level. Then the system can be regarded as a three-level system. The interaction within the three states leads to a level repulsion: If the interaction between the σ -mesonic mode and the $\sigma\sigma$ state becomes sufficiently strong as the system approaches the CP, the energy level of the sigma meson will be so strongly pushed down that it penetrates into the space-like region. To show that this scenario can be the case, we change the strength of the three-point vertex $\Gamma_{k,\sigma\sigma\sigma}^{(0,3)}$ by hand to investigate the behavior of the sigma-meson peak. The results in the cases of multiplying $\Gamma_{k,\sigma\sigma\sigma}^{(0,3)}$ by factors 0.8 and 1.02 are shown in Fig. 7. The position of the sigma meson goes up when the three-point vertex is weakened, whereas it exhibits a downward shift to a lower energy when the three-point vertex is slightly enhanced. This result suggests that the above interpretation in terms of a level repulsion can be correct.

Here it should be noted that our results exhibit a superluminal group velocity of the sigma-mesonic mode near the CP, as seen in Fig. 5 for $p = 100$ MeV at $\mu = 286.59$ MeV. Such an unphysical extreme behavior may be an artifact of our truncation scheme, in which some of the higher-order terms in the derivative expansion and the use of the three-dimensional regulator, Eqs. (10) and (11)¹, although a drastic softening of the sigma-mesonic mode may persist. We expect that such a drawback could disappear if one incorporates higher-derivative terms and/or uses a more sophisticated regulator respecting the covariance as much as possible. One of the most important higher-derivative terms may be the wave-function renormalization [35, 36], since the relative strengths of the modes should be properly taken into account when collective modes are dynamically generated in addition to the modes described by the fields existing in the bare Lagrangian, as is the case in the present work.

So far, we have concentrated on the spectral function in the sigma channel and seen interesting behaviors of it near the CP. It would be intriguing to examine whether the spectral function $\rho_\pi(\omega, p)$ in the pion channel shows any peculiar behavior near the CP. In contrast to ρ_σ , the dispersion relation of the pion mode stays in the time-like region and ρ_π hardly changes near the CP indicating that there is no critical behavior in the isovector pseudo-scalar modes both in the space-like and time-like regions.

¹We thank J.Pawlowski for pointing out this possibility.

4 Summary

In this note, we have demonstrated how to compute spectral functions in a relativistic system at finite temperature and density within the functional renormalization group approach. Our method is based on the local potential approximation (LPA) and Litim's optimized regulator in three dimension, which enable us to carry out an analytic continuation from imaginary to real frequency at the level of the flow equations for the two-point functions [16, 17]. We have also given a detailed numerical procedure including a stability condition [18].

We have applied the method to the two-flavor quark-meson model which is composed of light quarks, σ and π mesons as an effective realization of spontaneous chiral symmetry breaking and restoration of QCD at low energies. We have focused on the spectral function of the scalar (σ) channel in the vicinity of the CP which is located in large quark chemical potential and low temperature. In this region, an explicit breaking of the chiral symmetry due to a nonzero pion mass and the coupling of the quark density to the scalar channel give a non-trivial structure to the spectral function. Indeed, it was suggested that the particle-hole mode is enhanced near the critical point and thus the density fluctuations are the soft modes at the CP in a similar model calculation based on random phase approximation [29]. We have shown that the particle-hole mode has a growing support in the space-like region of the spectral function as the system approaches to the CP. Furthermore, we have found an anomalous dispersion relation of the σ meson; it penetrates into the space-like region as the system approaches to the CP, and then merges into the particle-hole mode. This anomalous softening of the σ meson might be attributed to a level repulsion between the σ meson and the two- σ mode.

Our results, obtained by calculating the spectral function of the scalar channel with FRG, may imply a novel picture of the soft modes of the QCD CP, which could influence the dynamical universality class. Since our method is based on LPA and the specific regulator function, the results should be examined by improving the truncation scheme, e.g., including the wave-function renormalization, and by exploring the regulator dependence. Nevertheless, our result paves the way for investigating emergent collective modes at finite temperature and density with the functional renormalization group.

Acknowledgments

T. Y. was supported by the Grant-in-Aid for JSPS Fellows (No. 16J08574). T. K. was partially supported by a Grant-in-Aid for Scientific Research from the Ministry of Education, Culture, Sports, Science and Technology (MEXT) of Japan (Nos. 16K05350, 15H03663), by the Yukawa International Program for Quark-Hadron Sciences. K. M. was supported by the Grants-in-Aid for Scientific Research on Innovative Area from MEXT (No. 24105008) and Grants-in-Aid for Scientific Research from JSPS (No. 16K05349). Numerical computation in this work was carried out at the Yukawa Institute Computer Facility.

References

- [1] C. Wetterich, Phys. Lett. B **301**, 90 (1993).
- [2] F. J. Wegner and A. Houghton, Phys. Rev. A **8**, 401 (1973).
- [3] K. G. Wilson, J. Kogut, Phys. Rept. **12**, 75 (1974).
- [4] J. Polchinski, Nucl. Phys. B **231**, 269 (1984).
- [5] J. Berges, N. Tetradis and C. Wetterich, Phys. Rept. **363**, 223 (2002).
- [6] J. M. Pawłowski, Ann. Phys. **322**, 2831 (2007).
- [7] H. Gies, Lect. Notes Phys. **852**, 287 (2012).
- [8] D. U. Jungnickel and C. Wetterich, Phys. Rev. D **53**, 5142 (1996).
- [9] J. Braun, H.-J. Pirner and K. Schwenzer, Phys. Rev. D **70**, 085016 (2004).

- [10] B.-J. Schaefer and J. Wambach, Nucl. Phys. A **757**, 479 (2005).
- [11] B. -J. Schaefer and J. Wambach, Phys. Rev. D **75**, 085015 (2007).
- [12] B. Stokić, B. Friman, and K. Redlich, Eur. Phys. J. C **67**, 425 (2010)
- [13] E. Nakano, B.-J. Schaefer, B. Stokic, B. Friman, K. Redlich, Phys. Lett. B **682**, 401 (2010).
- [14] K. Aoki, S. Kumamoto, and D. Sato, Prog. Theor. Exp. Phys. **2014**, 043B05 (2014).
- [15] K. Kamikado, N. Strodthoff, L. von Smekal and J. Wambach, Eur. Phys. J. C **74**, 2806 (2014).
- [16] R. A. Tripolt, N. Strodthoff, L. von Smekal and J. Wambach, Phys. Rev. D **89**, 034010 (2014).
- [17] R. A. Tripolt, L. von Smekal and J. Wambach, Phys. Rev. D **90**, 074031 (2014).
- [18] T. Yokota, T. Kunihiro and K. Morita, Prog. Theor. Exp. Phys. **2016**, 073D01 (2016).
- [19] M. Jarrell and J. Gubernatis, Phys. Rept. **269**, 133 (1996).
- [20] M. Asakawa, T. Hatsuda, and Y. Nakahara, Prog. Part. Nucl. Phys. **46**, 459 (2001).
- [21] H. J. Vidberg and J. W. Serene, Journal of Low Temperature Physics **29**, 179 (1977).
- [22] D. Dudal, O. Oliveira, and P. J. Silva, Phys. Rev. D **89**, 014010 (2014).
- [23] K. Fukushima and T. Hatsuda, Rept. Prog. Phys. **74**, 014001 (2011).
- [24] G. 't Hooft, Phys. Rev. Lett. **37** (1976) 8.
- [25] Y. Nambu, Phys. Rev. Lett. **4** (1960) 380.
- [26] Y. Nambu and G. Jona-Lasinio, Phys. Rev. **122**, 345 (1961); Phys. Rev. **124**, 246 (1961).
- [27] M. Gell-Mann, R. J. Oakes and B. Renner, Phys. Rev. **175** (1968) 2195.
- [28] T. Hatsuda and T. Kunihiro, Phys. Rept. **247** (1994) 221.
- [29] H. Fujii and M. Ohtani, Phys. Rev. D **70**, 014016 (2004).
- [30] D. T. Son and M. A. Stephanov, Phys. Rev. D **70**, 056001 (2004).
- [31] T. Kunihiro, Phys. Lett. B **271**, 395 (1991).
- [32] G. Baym and N. D. Mermin, J. Math. Phys. **2**, 232 (1961).
- [33] D. F. Litim, Phys. Rev. D **64**, 105007 (2001).
- [34] William H. Press, Saul A. Teukolsky, William T. Vetterling and Brian P. Flannery, *Numerical Recipes in C* (Cambridge University Press, 1992).
- [35] A. J. Helmboldt, J. M. Pawłowski and N. Strodthoff, Phys. Rev. D **91**, no. 5, 054010 (2015).
- [36] K. Kamikado and T. Kanazawa, JHEP **1403**, 009 (2014).